Numerical investigation of the effect of the VOF-CSF static contact angle boundary condition on the dynamics of small Eötvös number bubbles interacting with flat inclined surfaces

S. Senthil Kumar[a,*], Y. M. C. Delauré[a,*], D. B. Murray[b], B. Donnelly[b]

[a] *School of Mechanical and Manufacturing Engineering,Dublin City University, Glasnevin, Dublin, Ireland*
[b] *Department of Mechanical and Manufacturing Engineering, Trinity College Dublin, Ireland*

Abstract

The static contact angle is the only empiricism introduced in a Volume of Fluid - Continuum Surface Force (VOF-CSF) model of bubbly flow and it has previously been shown to have a relatively limited effect on the accuracy of velocity and shape predictions in the case of large gas bubbles sliding under inclined walls (1). Smaller ellipsoidal bubbles are known to display more unstable dynamic behaviours with repeating bouncing when sliding under inclined walls at certain wall inclinations (2). Under such conditions, the onset and significance of the bouncing component is strongly influenced by surface tension and the static contact angle is likely to have a more determining influence on the numerical prediction of the bubble dynamics. The present paper reports on this influence for an air bubble of equivalent diameter $D_e = 3.4mm$. The bubble Eötvös and Morton numbers are $Eo = 1.56$ and $Mo = 2x10^{-11}$ respectively, giving, according to the computational results, Reynolds and Weber numbers in the ranges 295-707 and 0.35-2 respectively. The computational results are achieved with a Piecewise Linear Construction (PLIC) of the interface. They are reviewed with reference to experimental measurements of bubble velocity and interface shape oscillations recorded

*Corresponding authors
Email addresses: sundararaj.senthilkumar2@mail.dcu.ie (S. Senthil Kumar), yan.delaure@dcu.ie (Y. M. C. Delauré)

using a high speed digital camera. Tests are performed at plate inclination angles $\theta \in \{10°, 20°, 30°, 45°\}$ to the horizontal and computational models consider three static contact angles $\theta_c \in \{10°, 20°, 30°\}$. The static contact angle has been found to have a significant effect on the bubble dynamics but to varying degree depending on the plate inclination. It is shown to promote lift off and bouncing when the plate inclination angle reaches 30° in a way that does not necessarily reflect experimental observations. A change to θ_c by as little as 5° is also shown to deform the bubble and to affect the slide velocity most notably at lower and higher plate inclination angles.

Keywords:
Gas-Liquid Flow; Sliding Bubble; Volume-of-Fluid; PLIC Method; SIMPLE Algorithm

---

1. Introduction

The flow of gas-liquid mixtures occurs in a wide range of engineering applications such as steam generation, electronic cooling and chemical reactors. The gas phase may result from phase change in power generation, thermal management or refrigeration or may be injected as part of the process to enhance mixing. The formation and free rise of gas bubbles in liquid have been studied extensively and are reasonably well understood (see (3) for a review). Navier Stokes solvers coupled with Volume of Fluid (VOF) and Continuum Surface Force (CSF) models have been shown to achieve accurate predictions of bubble shapes and terminal velocity for single bubbles in free rise (4), (5). By contrast, although bubble-wall interaction plays an important role in most bubbly flow processes, it has been the subject of relatively few studies. Several experimental and numerical investigations have considered the flow of Taylor bubbles or slug flow in tubes and rectangular channels where the gas phase fills a significant proportion of the space between the confining walls (1, 6). For this type of large bubble, a VOF-CSF model has been shown to achieve predictions of the bubble shape and slide trajectories and velocities which are in good agreement with experimental observations with little sensitivity to the static contact angle used to account for surface tension at solid boundaries. Other numerical studies with VOF solvers have achieved accurate models of Taylor bubbles in vertical pipes (7), (8) but in this case the bubble interface remains isolated from the solid boundaries by a thin liquid film. One experimental study by Maxworthy (9) has considered

large spherical cap bubbles sliding along inclined flat surfaces with no significant confinement.The Eötvös numbers ($Eo = g\Delta\rho D_e^2/\sigma$) considered were in the range 60-300. With Reynolds numbers ($Re = U_0 D_e/\nu$) greater than 650 this placed the free rise spherical-cap bubbles in the inviscid regime. Here, ρ and ν are the density and kinematic viscosity of the liquid, U_0 and De are the velocity and equivalent diameter of the bubble and σ is the surface tension of the liquid-gas interface. Maxworthy's study showed that steady inviscid flow theory also provides accurate predictions in the case of sliding bubbles, giving bubble shape characteristics and velocities which are within the experimental scatter. The suitability of approximate numerical models in this case can be explained by the fact that spherical cap and Taylor bubbles rise steadily with predominantly rectilinear trajectories which remain parallel to the confining wall.

Very different dynamic properties have been observed with smaller ellipsoidal bubbles rising under an inclined plate. Air bubbles of $4mm$ equivalent diameter ($Eo \simeq 2.16$) have been found to both slide and bounce at wall inclination angles of 65° and 77.5° (10). Smaller air bubbles of effective radius 1mm ($Eo < 1$) have been shown to lift off and bounce repeatedly without loss of amplitude for wall inclination angles greater than 55° (2). In the latter study, the existence of a thin lubrication film between the surface and the sliding bubble was also observed experimentally and corroborated by lubrication analysis. The bubble slide velocity was shown to decrease with a proportional thinning of the liquid film between the bubble and the surface as the inclination angle is reduced. Experimental observations suggested that for sufficiently low inclination of the flat plate, the drainage of the thin film continues until it reaches a few micrometers and the van der Waals forces become predominant (2). At that stage the gas-liquid interface may reconnect with the solid surface affecting the process of energy restitution due to the bubble deformation. Because of the difficulty in resolving both the microscopic liquid film and the larger scale flow, most numerical studies have not modelled the microscopic Van Der Walls interaction between the fluids and solid surfaces (11). Surface tension is instead generally modelled by imposing the apparent contact angle between the interface and the solid surface (12) along with a no slip boundary condition for the mixture velocity. Using the face normal velocity component to approximate the flux of one of the phases means that the contact line typically moves relative to the solid surface avoiding the stress singularity that would otherwise exist at the wall due to the no slip boundary condition. This approach, however, also means

that the solution cannot be grid independent.

The majority of computational studies of bubble flow have relied on the VOF (13) or the Level-Set methods (14) to model the two-phase incompressible flow, accounting for surface tension through the Continuum Surface Force (CSF) model (15). The only numerical study of ellipsoidal bubble sliding along a flat inclined surface known to the authors is a two-dimensional study relying on a Level Set Method (16). The study considered the effect of the Eötvös and Reynolds numbers as well as the surface inclination angle but did not assess the model sensitivity to the interface contact line model and considered relatively modest density and viscosity ratios, i.e. $\rho_g/\rho_l = 0.01$ and $\mu_g/\mu_l = 1$ respectively. The present study uses a VOF-CSF model coupled to a SIMPLE Navier Stokes solver to assess the suitability of the static contact angle formulation by studying the sensitivity of results to the input parameters and by comparing predictions with experimental measurements. The two-fluid mixture studied is air-water with $\rho_g/\rho_l = 1.225 \cdot 10^{-3}$ and $\mu_g/\mu_l = 0.018$. The bubble studied is larger than that considered by (2) but is still in the ellipsoidal regime with an initial diameter of $D_e = 3.4mm$ and an Eötvös number $Eo = 1.55$. The study considers conditions where the bubble slides along the surface without repeated bouncing so tests are performed at plate inclination angles $\theta \in \{10°, 20°, 30°, 45°\}$ to the horizontal. The computational study considers three static contact angles $\theta_c \in \{10°, 20°, 30°\}$.

2. Numerical formulation

2.1. The governing equations

The governing equations for unsteady, incompressible, immiscible two-fluid VOF-CSF model include the continuity, momentum and VOF advection equations. They are written as:

$$\nabla \cdot \mathbf{V} = 0 \tag{1}$$

$$\rho \frac{\partial(\mathbf{V})}{\partial t} + \nabla \cdot (\rho \mathbf{V}\mathbf{V}) = -\nabla p + \nabla \cdot \tau + \rho \mathbf{g} + \mathbf{F}_b \tag{2}$$

$$\frac{\partial f}{\partial t} + \nabla \cdot (f\mathbf{V}) - f(\nabla \cdot \mathbf{V}) = 0 \tag{3}$$

where ρ is the fluid density, $\mathbf{V}$ the fluid velocity vector, p the scalar pressure, τ the viscous stress tensor, $\mathbf{F_b}$ a body force, $\mathbf{g}$ the acceleration due to

gravity and f the volume fraction. Although the incompressible continuity equation is used, spatial variations in density are accounted for in the momentum equations. In Eq. 3, the velocity divergence, $\nabla \cdot \mathbf{V}$ is retained since its discrete approximation is not zero but a function of the continuity convergence tolerance (17). The nonlinear advection term is written in conservative form and the viscous stress tensor τ is defined according to the Newtonian formulation:

$$\tau = 2\mu S. \qquad S = \frac{1}{2}\left[(\nabla \mathbf{V}) + (\nabla \mathbf{V})^T\right] \tag{4}$$

where S is the rate-of strain tensor and μ is the coefficient of dynamic viscosity. The mixed properties used in Eq. (2) can be defined as:

$$\rho = f\rho_g + (1-f)\rho_l \tag{5}$$
$$\mu = f\mu_g + (1-f)\mu_l \tag{6}$$

where the subscript l denotes liquid and the subscript g denotes gas. The scalar function f is generally known as the volume fraction or VOF function. The discrete representation of the function f is equal to 1 in cells fully filled by the liquid phase and equal to 0 in cells filled by the gas phase but takes a value bounded by 0 and 1 in cells where the interface lies.

2.2. Navier Stokes solver

The two-dimensional (2D) momentum and mass conservation equations are solved iteratively using a SIMPLE algorithm (18) modified to include the VOF advection equation. The equations are discretised by Finite Volumes on an orthogonal staggered C-grid, where the pressure and fluid properties are evaluated at the cell centers (i, j) while the velocity components $u_{i+1/2,j}$ and $v_{i,j+1/2}$ are evaluated at the centres of the cell faces which are perpendicular to the x and y directions respectively. The convective flux coefficients are derived by a first order upwind scheme while the diffusive flux coefficients are obtained by central differencing and the equations are discretised in time by implicit first order Euler differencing. The linearised momentum equations are solved using a Krylov subspace, iterative method and the pressure correction equation is solved with a Multigrid solver. For any given numerical test, the same iterative method is used as a smoother for the momentum

equations and for the Multigrid scheme at all grid levels. The iterative solver considered is an RILU preconditioned BiCGStab with an RILU parameter of 0.95. The Multigrid iterations involve repeated calls of the μ - cycles until the specified convergence criterion is met. The absolute residuals used to test convergence are evaluated using a l2 norm and a continuity residual lower than or equal to 10^{-4} is used to test convergence at each time step.

2.3. Surface tension force estimation

The dynamic stress balance is realised through the CSF - ALE model (15) incorporated in the momentum equation by introducing a volume force $\mathbf{F}_b$. This localised volume force is calculated from the volume fraction data by

$$\mathbf{F}_b = \sigma\kappa(x)\widetilde{\mathbf{n}}\frac{\nabla\widetilde{f}(x)}{[f]}\frac{\rho(x)}{[\rho]} \tag{7}$$

where κ is the curvature of the interface and the $\sim$(tilda) denotes filtered(smoothed) values and the square bracket denotes the difference between the maximum and the minimum values of the function inside the brackets and $\rho(x)$ is the local value of the density obtained by Eq. (5).

The interface characteristic parameters, the outward normal vector $\widetilde{n}$ and curvature κ, are calculated as

$$\widetilde{\mathbf{n}} = (\widetilde{n}_x, \widetilde{n}_y) = -\nabla f, \qquad \hat{\mathbf{n}} = \frac{\widetilde{\mathbf{n}}}{|\widetilde{\mathbf{n}}|} \tag{8}$$

$$\kappa = (\nabla \cdot \hat{\mathbf{n}}) = -\frac{1}{\widetilde{\mathbf{n}}}\left[\left(\frac{\widetilde{\mathbf{n}}}{|\widetilde{\mathbf{n}}|}\cdot\nabla\right)|\widetilde{\mathbf{n}}| - (\nabla\cdot\widetilde{\mathbf{n}})\right] \tag{9}$$

Brackbill et al. (15) have rewritten the curvature in terms of $\widetilde{\mathbf{n}}$ and $|\widetilde{\mathbf{n}}|$ to ensure that the main contribution from the finite difference approximation of κ comes from the center of the transition region rather than the edges. This can be achieved by an Arbitrary Lagrangian Eulerian (ALE)-like scheme or MAC method. In both approaches, the color function is chosen to be the fluid density, which resides at the centre of the control volumes denoted using the indices i, j. The curvature $\kappa_{i,j}$ therefore also will be cell-centered. Both approaches were tested and it was found that the ALE scheme works better than the MAC method giving more stable flows and is used in this study.

As the governing equations are discretised on the staggered grid and the surface tension forces have to be calculated at the cell faces for the momentum equations, it is found that an averaging of F_b from cell centers gives better results.

The CSF method has the ability to use the smoothed or mollified VOF function $\widetilde{f}_{i,j}$ for the calculation of the curvature $\kappa_{i,j}$ in the volume force of Eq. (7), which is different from the unsmoothed function $f_{i,j}$ used to calculate the normal vector in Eq. (8). This enables the algorithm to calculate a smoother curvature for accuracy, and has been found to decrease the number of pressure solution iterations.

The smoothed VOF function is computed by convolving f with a B-Spline of degree l ((19, 15)), $\beta^{(l)}(|X' - X|; H)$, (with l=2) where $\beta^{(l)} \neq 0$ only for $|X' - X| < (l + 1)h/2 = 3h/2$. The smoothed VOF function is given by:

$$\widetilde{f}_{i,j} = \sum_{i',j'=1}^{k} f_{i,j}\beta^{(l)}\left(x'_{i',j'} - x_{i,j}\ ; h\right)\beta^{(l)}\left(y'_{i',j'} - y_{i,j}\ ; h\right) \tag{10}$$

where the sum gathers contributions from the nine values (for l=2 in 2-D) of $f_{i,j}$ within the support of β^2. Here, this formulation becomes simply:

$$\widetilde{f}_{i,j} = \frac{9}{16}f_{i,j} + \frac{3}{32}\left(f_{i+1,j} + f_{i-1,j} + f_{i,j+1} + f_{i,j-1}\right) \tag{11}$$

$$+\frac{1}{16}\left(f_{i+1,j+1} + f_{i+1,j-1} + f_{i-1,j+1} + f_{i-1,j-1}\right) \tag{12}$$

This formula may be applied iteratively by multiple passes through the mesh for increased degrees of smoothing. Tests have shown that one to three passes are optimal, with most calculations carried out with one pass. A single iteration was used in this study.

The face centered values of $\mathbf{F}_{b\,i,j}$ at the right and top faces are required for the momentum equations and are calculated from cell centered values:

$$\mathbf{F}_{bi+0.5,j} = 0.5 \times (\mathbf{F}_{bi+1,j} + \mathbf{F}_{bi,j}) \tag{13}$$

$$\mathbf{F}_{bi,j+0.5} = 0.5 \times (\mathbf{F}_{bi,j+1} + \mathbf{F}_{bi,j}) \tag{14}$$

2.4. The interface tracking algorithm

The interface tracking algorithm advances the solution of Eq. (3) in time. It requires first that an approximation to the interface is reconstructed from the known distribution of $f_{i,j}^n$ at time $t = n\Delta n$. In this work, the Piecewise Linear interface calculation (PLIC) method due to Youngs (20) is used. It represents the interface by line segments positioned to conserve the volume fraction and to satisfy Eq. 8.

The VOF advection equation (Eq. 3) is solved after the Navier Stokes equations using the discrete velocity and the reconstructed line description to approximate flux of f across the cell faces. A first order un-split advection algorithm (17), which is based on the standard conservative finite difference update of Eq. (3) provides the updated volume fraction $f_{i,j}^{n+1}$ from its value $f_{i,j}^n$ at time $t^n = n\Delta t$:

$$f_{i,j}^{n+1} = f_{i,j}^n + \frac{\Delta t}{\Delta x}\left[F_{i-1/2,j} - F_{i+1/2,j}\right] + \frac{\Delta t}{\Delta y}\left[G_{i,j-1/2} - G_{i,j+1/2}\right] + \Delta t f_{i,j}^n \left[\frac{(u_{i+1/2,j} - u_{i-1/2,j})}{\Delta x} + \frac{(v_{i,j+1/2} - u_{i,j-1/2})}{\Delta y}\right] \quad (15)$$

where $F_{i-1/2,j}$ and $G_{i,j-1/2}$ for example are the approximated flux of f at the west and south face of the (i,j)th cell respectively. Ordinarily the last term in Eq. 15 would be zero if the continuity equation was satisfied but it has been found desirable to include it numerically to account for the effect of approximate convergence to the chosen tolerance.

2.5. The static contact angle boundary condition

When a bubble is in contact with a solid surface, surface tension influences the angle formed between the air-water interface and the solid surface. For a static problem, the so-called apparent contact angle can be measured relatively easily and is known to be a property of the two fluids and of the solid surface. If the bubble is in motion, the contact angle is also influenced by the dynamics of the interface, which itself depends on the interaction between inertia, surface tension and buoyancy forces. This dependence however is neglected in computational models, when a fixed and constant contact angle, written θ_c, is imposed rather than being a result of force balance. This static contact angle formulation provides a wall boundary condition for the

volume fraction function f. It is used instead of Eq. 8 to calculate the normal vector $\hat{\mathbf{n}}$. The surface curvature and then the surface tension force are evaluated as normal from Eq. 9 and Eq. 7. This means that the contact angle is not strictly imposed but rather it is its influence on the momentum equation which is accounted for. This means that in a steady static case, the interface angle will converge to the imposed static contact angle θ_c, but in the unsteady case of a sliding bubble the interface angle will vary dynamically as a result of force balance.

3. Problem definition

3.1. Computational setup

The 2D computational domain consist of a 80mm by 20mm rectangle which includes a rectangular obstacle used to represent the immersed flat plate (see Fig. 2.b for example). The axes of symmetry of the two rectangles are parallel to each other. The domain is initially filled with stationary water and an air bubble is intialised at $t = 0s$ as a circular patch with its centre positioned at a distance of $6.5mm$ measured perpendicular to the lower surface of the plate. In cells containing the interface, the volume fraction is estimated by approximating the circle intersection with the cell using a piecewise linear reconstruction of the interface. This minimises curvature variations and associated stability issues at the first time steps. No-slip boundary conditions are applied at all confining walls and inclined plate surfaces. Four plate inclination angles θ of 10°, 20°, 30° and 45° from the horizontal direction are tested. The parameters used for these simulations are listed in Table 1. Computations were performed with a grid of 800×200 cells and a time step of $10^{-4}s$. The mesh decomposes the initial bubble with 34 cells across the bubble diagonal, which was shown to be sufficient to provide free rise velocity predictions in agreement with correlations from (21). The mesh is uniform and orthogonal with square cells of width and height equal to 10^{-4} m. This gives a maximum Courant number based on the maximum bubble velocity approximately equal to 0.2.

3.2. Experimental setup

Physical experiments were performed with water at $20 \pm 0.5°C$ giving fluid properties which approach those described in Table 1. Although the experimental results are used to provide reference data for the assessment of the computational results, it is important to highlight the two fundamental

Table 1: Test parameters

Parameters	Symbols	Values	Units
Liquid density	ρ_l	1000	kg/m^3
Liquid viscosity	μ_l	0.001	$kg/m \cdot s$
Gas density	ρ_g	1.225	kg/m^3
Gas viscosity	μ_g	$1.8 \cdot 10^{-5}$	$kg/m \cdot s$
Surface tension	σ	0.0728	N/m
Acceleration Gravity	$\mathbf{g}$	9.81	m/s^2
Contact angles	θ_c	20°, 25°, 30°	-
Plate inclination angle	θ	10°, 20°, 30°, 45°	-
Plate length, width	L_p, W_p	0.073, 0.002	m
Tank length, width	L, W	0.08, 0.02	m

differences which characterise the two sets of results. First the computational model rely on a two dimensional formulation and cannot resolve the complex three dimensional vortices shed by the bubble, experimental tests however have shown that the bubble slide trajectory is predominantly confined to a 2D plane perpendicular to the plate. Experimental measurements and data analysis are performed assuming that the motion is indeed confined to a plane. A NAC Hi-Dcam II digital high-speed colour camera (max resolution 1280 x 1024 pixels, dependent on frame rate and image size) is used to capture the bubble position and its boundary. A frame rate of 250 fps with an exposure time of 0.001s were found to be suitable. For bubble tracking, two images are required in order to locate a bubble in any specific image; these are the background image and an image containing the whole bubble. Both images are first converted to HSV colourspace, working only on the intensity part of the images. The bubble is isolated by subtracting the image containing the bubble with the background image. Any element not common in both images shows up as a value greater than one, with all common elements at unity. This is deemed the enhanced image. The enhanced image is converted to binary by defining a threshold value, calculated by using maximum and minimum enhancement values, everything above this value is assigned a binary value one (white), everything else is assigned zero (black). It is then possible to analyse the bubble properties including the projected surface area, the centroid position, the centroid velocity and the bubble con-

tour within the plane of motion. The area of the bubble is used to find the equivalent diameter of the bubble $D_e = \sqrt{4 \times Area/\pi}$. Since this diameter is calculated from a 2D projection we can expect variations as the bubble detaches from the needle and slides or bounces along the plate after impact. These variations however were found to be most significant just after detachment from the needle tip and were generally less than 3% during the slide. 3D measurements of the equivalent diameter of the bubble projection also showed a slow increase during the slide indicating that the bubble stretch in the direction perpendicular to the plane of measurement reduces gradually with time. We have assumed a constant equivalent diameter of $D_e = 3.4mm$ in the 2D simulation which closely approximates the observed experimental diameter at the initial stage of the bubble slide.

Another difficulty relates to the injection of the bubble which needed to replicate as closely as possible the initial conditions described in Section 3.1. Accurate bubble volume injection is achieved by using an infusion pump and a surgical syringe (kdScientific model 200). From this, air is supplied to a machined medical needle, with an external diameter of $2.1mm$, at a constant flow rate of $0.05ml/min$ which is sufficiently slow to avoid any momentum being transferred to the bubble at detachment. The needle is positioned so that it is parallel to the direction of gravity, for all plate inclinations and with its tip at a distance from the plate which enable a bubble detachment also at a distance of $6.5mm$ from the plate. Detachment, however, is controlled by surface tension at the intersection between the bubble interface and the needle so that the initial bubble shape is not spherical but instead is stretched towards the needle and along the needle axis as illustrated in Fig. 2.

4. Results

4.1. Assessment of Static Contact Angle Numerical Boundary Condition

Observations of sliding bubbles obtained from experiments for the four plate inclination angles under consideration showed that the apparent contact angle that the sliding interface forms with a solid surface when in contact with it, is generally within the range $20° - 30°$. Similar apparent contact angles were observed with a static bubble under a horizontal plate. The present assessment of the effect of the static contact angle on the VOF-CSF models considers three static contact angles within this range, i.e. ($\theta_c = \{20°,\ 25°,\ 30°\}$).

There are three main effects which can be anticipated to impact on the shape and dynamics of the numerical bubble in ways that do not necessarily represent actual physical processes. First, observations discussed in the following subsections indicate that by increasing the contact angle, the bubble is forced to stretch in the direction perpendicular to the solid surface. This impacts on the bubble hydrodynamic profile and can be expected to influence pressure distribution around the bubble. Second, as soon as a small volume fraction of air enters a wall adjacent cell, the model assumes that the interface is in contact with the wall and surface tension attempts to impose an orientation to the interface as a function of the contact angle. The resultant force attracts the bubble towards the wall and may hinder lift off from the surface and dampen the bubble bounce. This attractive force is a function of the mesh size rather than a representation of the physical intermolecular forces. The third effect results from the latter one. Since the contact angle formulation promotes reconnection of the interface with the solid surface, the thin liquid layer that has been observed experimentally (2) cannot be captured accurately. Physically, the existence or otherwise of the lubrication film can be expected to affect the way surface tension energy is restored after deformation of a bouncing or sliding bubble with shape oscillations. The numerical formulation will tend to suppress this.

The purpose of the series of tests reported here is to assess the global effect of changes to θ_c by comparing changes to the bubble shape and its behaviour as well as the bubble slide velocity. The observations presented focus on the sliding part of the trajectory ignoring the more complex transient phase following impact with the plate. Computational results are also assessed with reference to experimental observations and measurements. Because of the 2D nature of the computations, this comparison is done primarily to provide a reference to the expected physical behaviour without seeking to evaluate precisely the relative difference between experimental and computational results. From a first inspection, no simple relationship between the slide velocity average, the contact angle and the plate inclination can be found and it is clear that multiple interacting factors affect the dynamics of the bubble as predicted by the numerical model. The four plate inclination angles are considered in turn as they provide some insight into three somehow distinct phenomena.

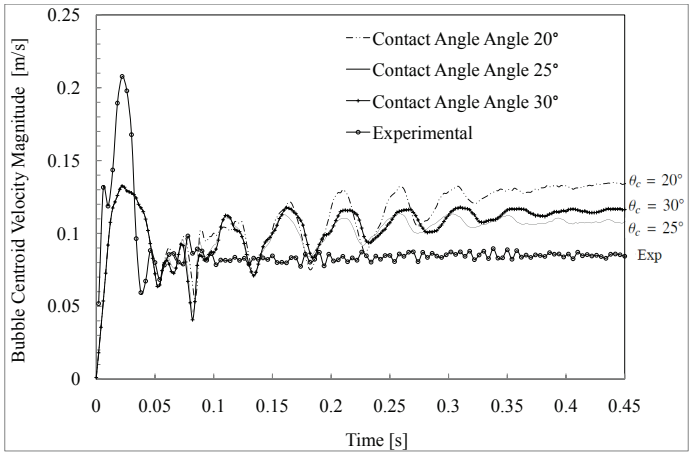

Figure 1: Velocity of bubble centre of gravity starting at injection for $\theta = 10°$

4.2. Gravitational flattening with a plate inclination angle $\theta = 10°$

When the plate is inclined at an angle $\theta = 10°$, the slide velocity decreases slightly as the contact angle is reduced from 30° to 25° (see Fig. 1) but increases significantly when it is further decreased to 20°. This is most obvious at $t = 0.45s$. In the present case, the low inclination angle of the plate means that the flattening of the bubble under the plate due to buoyancy is most significant compared to all other plate inclinations and tends to reduce the pressure drag experienced by the sliding bubble by minimising the frontal cross section area. Increasing the contact angle can be observed to stretch the bubble in the direction perpendicular to the plate surface countering the buoyancy effect on drag. Comparing the numerical predictions as the contact angle is increased from 20° to 25° shows that this results in a decrease in the slide velocity. This observation is consistent with the earlier conclusion that an increase in the frontal cross section area leads to higher drag and lower slide velocity. A further increase in the contact angle however is found to reduce the velocity, although by a lesser extent. Figs. 2b, c and d show a slight gradual tilting of the bubble forward as the bubble is stretched in the direction perpendicular to the plate by increasing the contact angle. The increase in slide velocity can be assumed to infer that this elongated and tilted bubble shape predicted with $\theta_c = 10°$ presents a more more favorable hydrodynamic profile and hence a decrease in the added mass and inertia of the bubble which allows a more rapid acceleration. The slide velocity is clearly shown here to be very sensitive to the contact angle and observations suggest that this is due to surface tension forces being of a similar order of

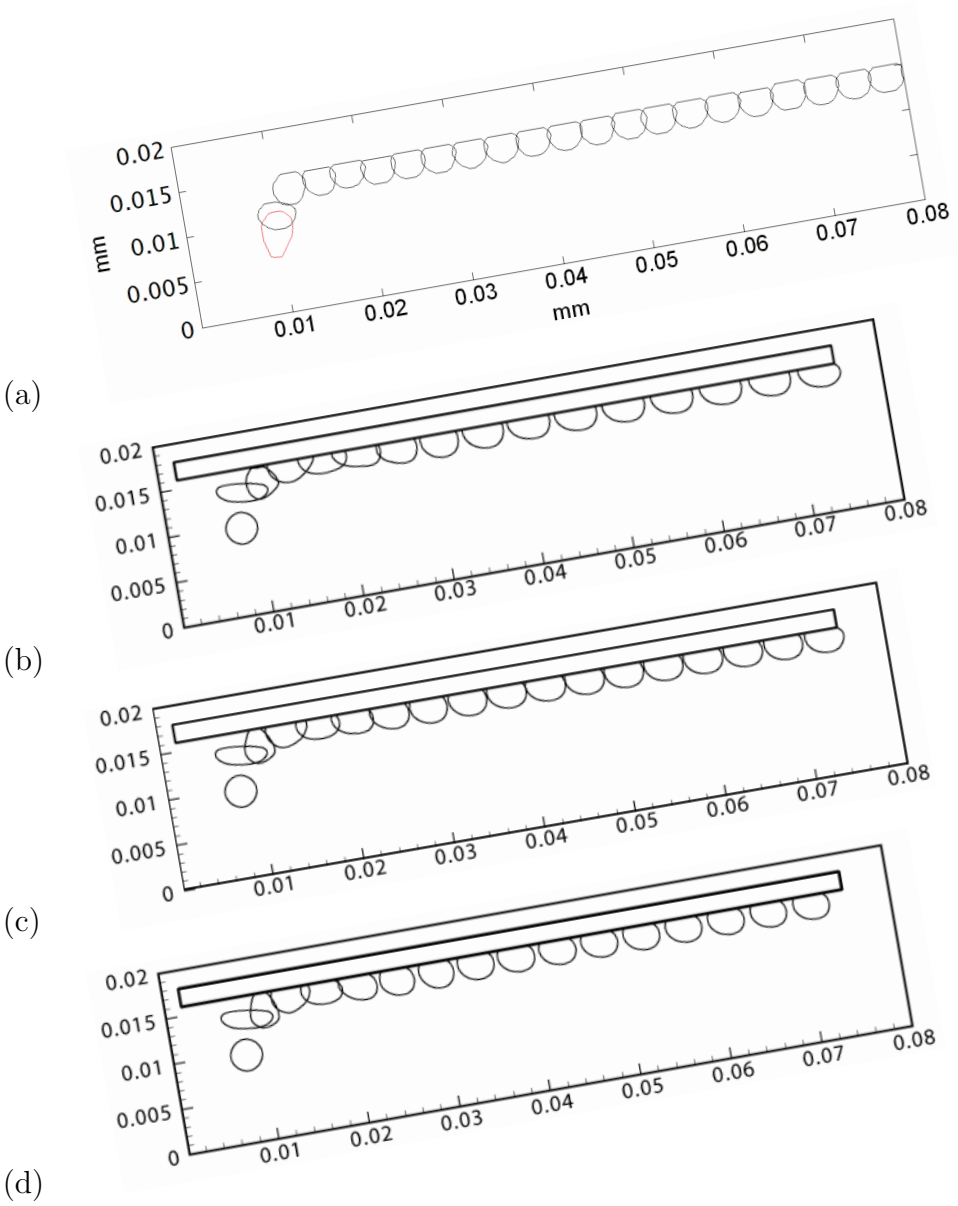

Figure 2: Bubble interface plots with plate inclination angle $\theta = 10°$ at time intervals $\Delta t = 0.04s$; (a) Experimental; Computational with varying contact angle (b) $\theta_c = 20^o$, (c) $\theta_c = 25^o$ and (d) $\theta_c = 30^o$.

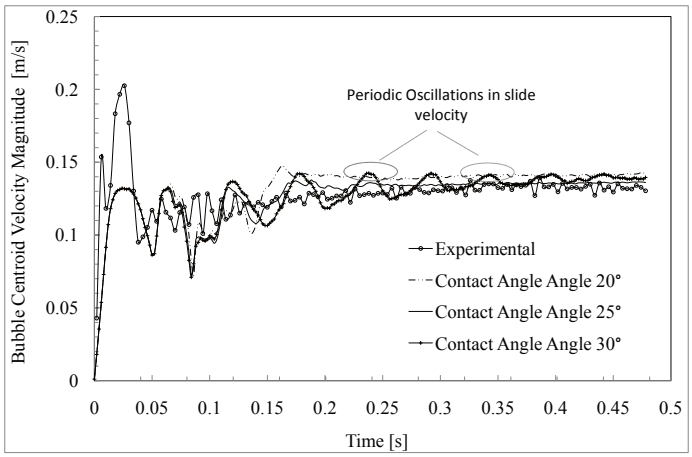

Figure 3: Velocity of bubble centre of gravity starting at injection for $\theta = 20°$

magnitude as pressure and buoyancy forces.

Periodic oscillations in the velocity are noticeable with all contact angles but these are shown to decay with time so that the slide velocities converge to relatively steady values at $t = 0.45s$. The initial oscillations reach their highest value shortly after collision and can be seen on Fig. 2 to occur at the same time as oscillations in the bubble shape as surface tension energy is restituted during the slide along the plate surface. They are clearly triggered by the bubble collision and the resulting deformation and can be assumed to be sustained by the interchange between the kinetic energy of the liquid motion, the surface tension energy and the gravitational potential energy. The relatively sustained pattern of oscillations suggests that surface, potential and kinetic energies are of comparable magnitude in the present case. The damping with time of both shape and velocity oscillations can be attributed to viscous dissipation which appears not to be significantly affected by the static contact angle.

4.3. Uniform slide with a plate inclination angle $\theta = 20°$

When the plate is inclined at $\theta = 20°$ the trends in the bubble velocity predicted by the numerical model, with the different contact angles, are quite different from those observed with $\theta = 10°$ as shown in Fig. 3. The bubble velocities are almost equal for $\theta = 25°$ and $30°$ and oscillations after impact are very quickly dampened and the velocity plots shows equally rapid con-

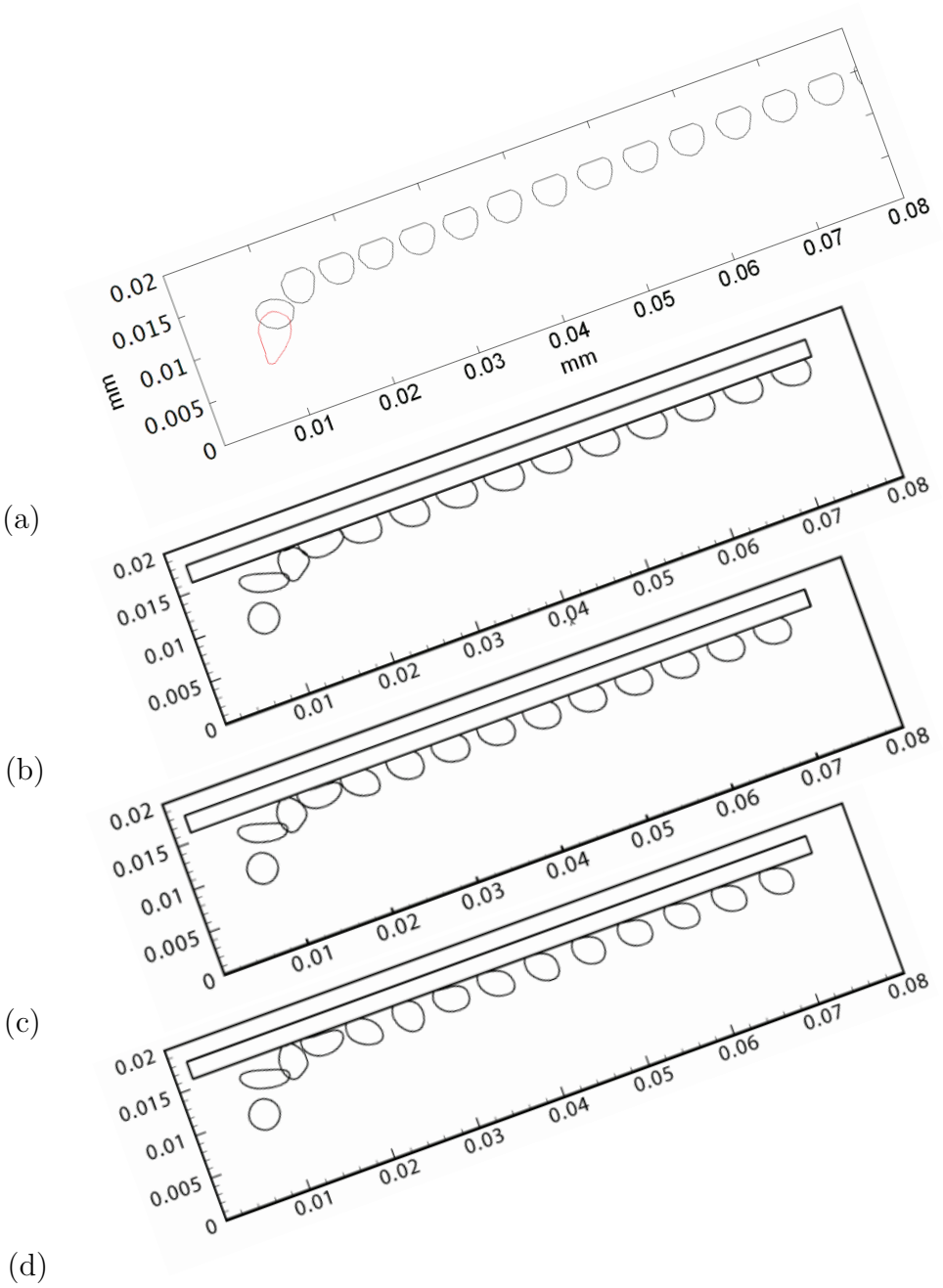

Figure 4: Bubble interface plots with plate inclination angle $\theta = 20°$ at time intervals $\Delta t = 0.04s$; (a) Experimental; Computational with varying contact angle (b) $\theta_c = 20^o$, (c) $\theta_c = 25^o$ and (d) $\theta_c = 30^o$.

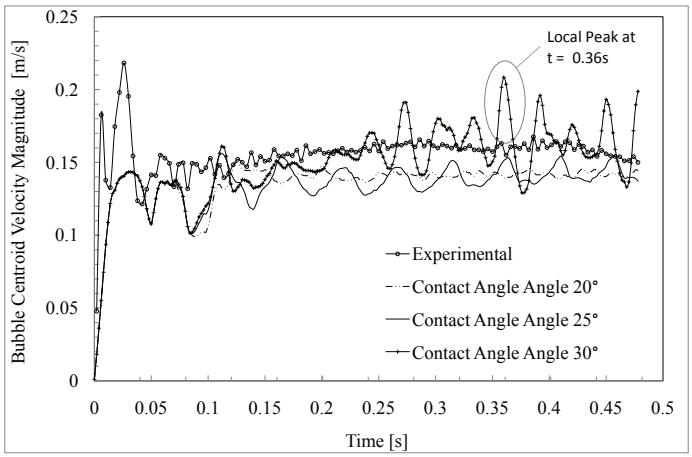

Figure 5: Velocity of bubble centre of gravity starting at injection for $\theta = 30°$

vergence to a near steady value. This is not the case with the larger contact angle of $\theta_c = 30°$, for which the velocity oscillations are shown to decay more slowly. The contour plots on Fig. 4.d show that the contact angle does indeed have a noticeable effect on the stretching of the bubble away from the plate surface. As a result the bubble is shown to rock forth and back while maintaining a slight forward tilt. Since the stretching does not lead to a reduction in the velocity as observed with the lower plate inclination, it must be assumed that the lesser significance of gravitational flattening of the bubble allows it to evolve into a more hydrodynamically profiled shape thereby balancing the increased transverse surface area and related drag due to increased contact angle. Comparison with the experimental velocity suggest that the slide velocity is over-predicted but only slightly. A comparison of the experimental and numerical interface plots, however, are giving the first indication of the non negligible effect that the contact angle has on the accuracy of shape prediction. This is most notable with $\theta_c = 30°$, in which case the bubble assumes a shape which is clearly different from the experimental bubble. These differences will be discussed in more detail in Sec. 4.4.

4.4. The onset of numerical bouncing at a plate inclination angle $\theta = 30°$

When the plate is inclined at $\theta = 30°$ the trends in the bubble velocity predicted by the VOF-CSF model show little difference between $\theta_c = 20°$ and $\theta_c = 25°$ as shown in Fig. 5. However, large velocity oscillations appear with $\theta_c = 30°$. These can be linked to the onset of bubble lift off from the solid sur-

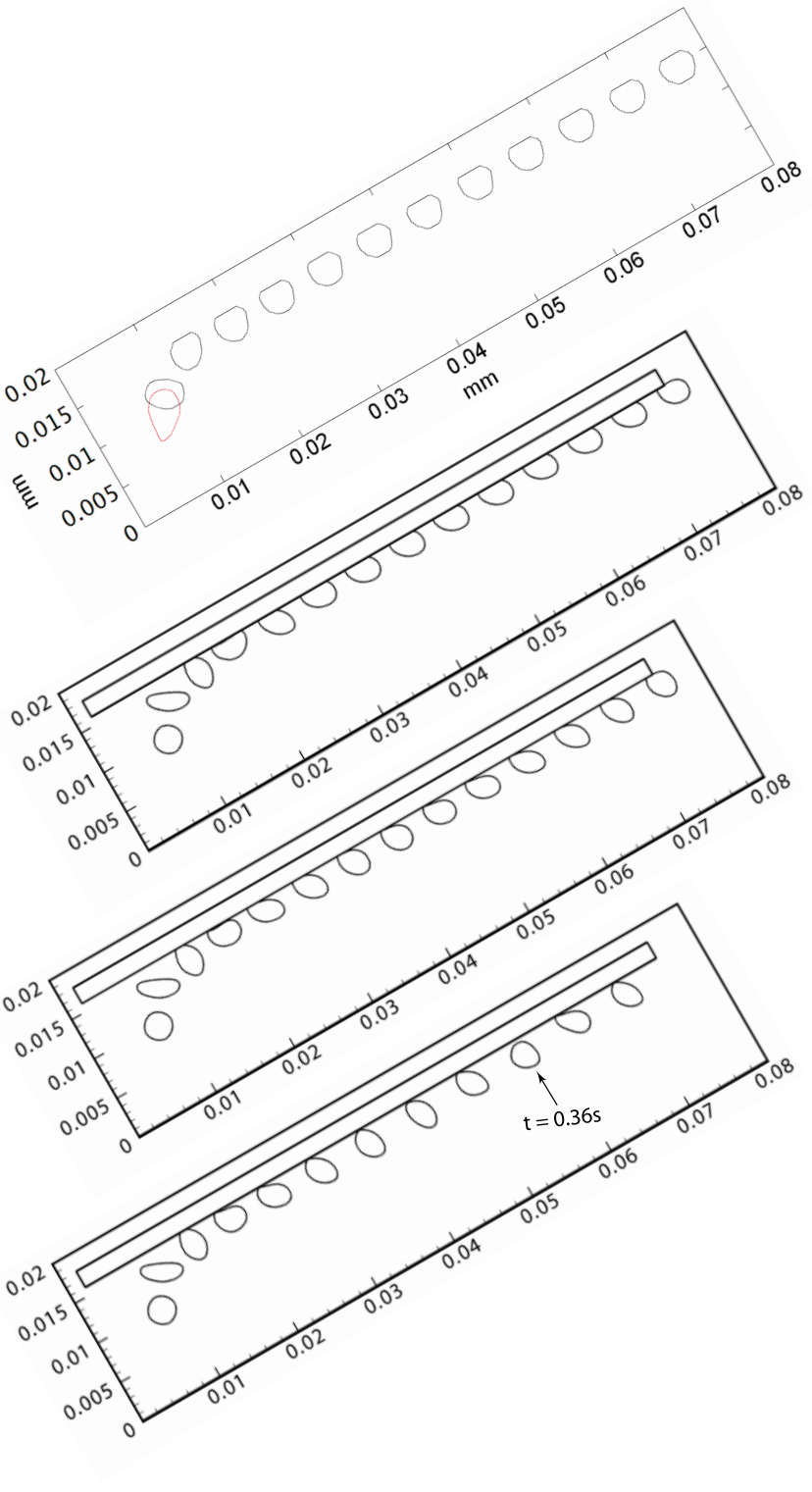

Figure 6: Bubble interface plots with plate inclination angle $\theta = 30°$ at time intervals $\Delta t = 0.04s$; (a) Experimental; Computational with varying contact angle (b) $\theta_c = 20^o$, (c) $\theta_c = 25^o$ and (d) $\theta_c = 30^o$.

face and the repeated bouncing motion that follows. It can be seen that once the bubble detaches from the surface, its velocity reaches a local maximum. For example the 10^{th} contour plot shown in Fig. 6.d, which corresponds to the time $t = 0.36s$, can be matched to the velocity peak at the same time in Fig. 5. Interestingly, the velocity is similar to that predicted with the other contact angles when the bubble slides without bouncing. These results however make it clear that if one is interested in the convective mixing induced by the bubble, the bouncing component can have a very significant effect on the surrounding flow. The largest oscillations modelled in this case are approximately 45% of the velocity average. The onset of lift off can be explained by stretching of the bubble due to an increase in the contact angle. As the static contact angle is increased, the bubble shape is increasingly stretched away from the plate surface with a corresponding reduction in the apparent contact area between the bubble and the plate. This can be observed by comparing Figs. 6b-d. These plots also show how the bubble stretches and leans forward when the contact angle is increased forcing water between the bubble and the solid surface which in turns leads to a detachment of the bubble from the wall.

By contrast the experimental bubble is shown in Fig. 6.a to slide along the plate without detaching. The bubble shape is also characterised by a fore-aft symmetry which is maintained for most of the slide. The only contact angle which gives reasonable comparison showing less stretching of the bubble shape in the streamwise direction is the $\theta_c = 20°$, while the larger θ_c the more the bubble deforms. Similar observations can be made from results with a plate inclined at 40° (not shown here). It is worth noting, as discussed in Sec.4.1, that what appears to be a contact area between the bubble and the solid surface in Fig. 6.a is in fact a lubrication area. It corresponds to the portion of the bubble which is flattened by the plate and provides a channel for the lubrication film. Lubrication analysis has shown ((2)) that the lift force induced by this lubrication flow is sufficient to balance buoyancy force from the bubble and avoid direct contact between the bubble and the solid surface when the bubble slides along the plate.

4.5. The onset of experimental bubble shape distortion at a plate inclination angle $\theta = 45°$

Increasing the plate inclination by increments of 5° in the experiments shows that unsteady changes in the bubble shape following collision with the plate start occurring at a surface inclination $\theta = 45°$. Below this angle,

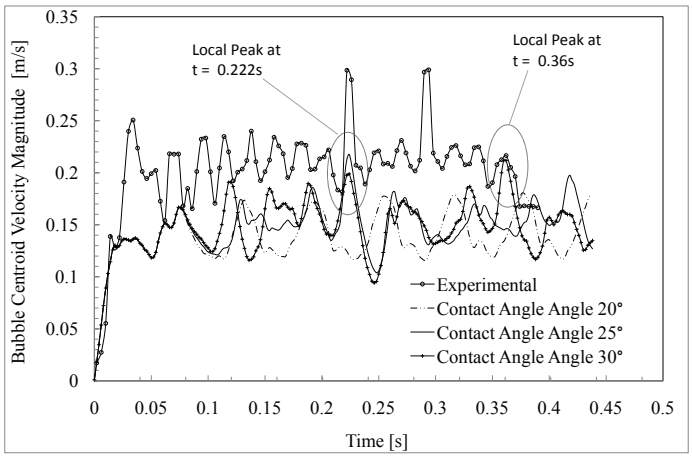

Figure 7: Velocity of bubble centre of gravity starting at injection for $\theta = 45°$

including at $\theta = 40°$, the bubble settled into a steady shape with fore-aft symmetry as illustrated for example on Fig. 6.a. At $\theta = 45°$ the bubble shape is shown to stretch and rock forth and back during the slide (see Fig. 8.a) leading to periodic oscillations in the velocity of the bubble centre of gravity (see Fig. 7). The bubble is also shown to detach from the surface most notably at $t = 0.16s$ but also at $t = 0.24s$ and $t = 0.36s$, although the amplitude of the bounce appears to reduce along the slide. By comparison with lower plate inclination, the apparent lubrication area between the sliding bubble and the solid surface (when not detached from the surface) has also reduced significantly. These observations suggest that further increase in the plate inclination will lead to sustained bouncing of the bubble which in (2) was shown to occur for surface inclination greater than 55°.

Comparing the experimental results with the computational predictions, it is clear again that the static contact angle formulation induces more stretching of the bubble. With $\theta_c = 30°$ (Fig. 8.d) the bubble detaches fully from the surface and bounces repeatedly but with the smallest contact angle $\theta_c = 20°$ (Fig. 8.b) it remains attached to the surface throughout the slide albeit only by a small section which holds the bubble back leading to a fore-aft stretching which is much larger than observed experimentally. This observation is consistent with earlier discussions (Sec. 4.1) on the effect of the numerically induced attraction due to the static contact angle boundary condition. Note that the numerical formulation means that if the interface remains attached to the solid surface it will be advected at the mean velocity

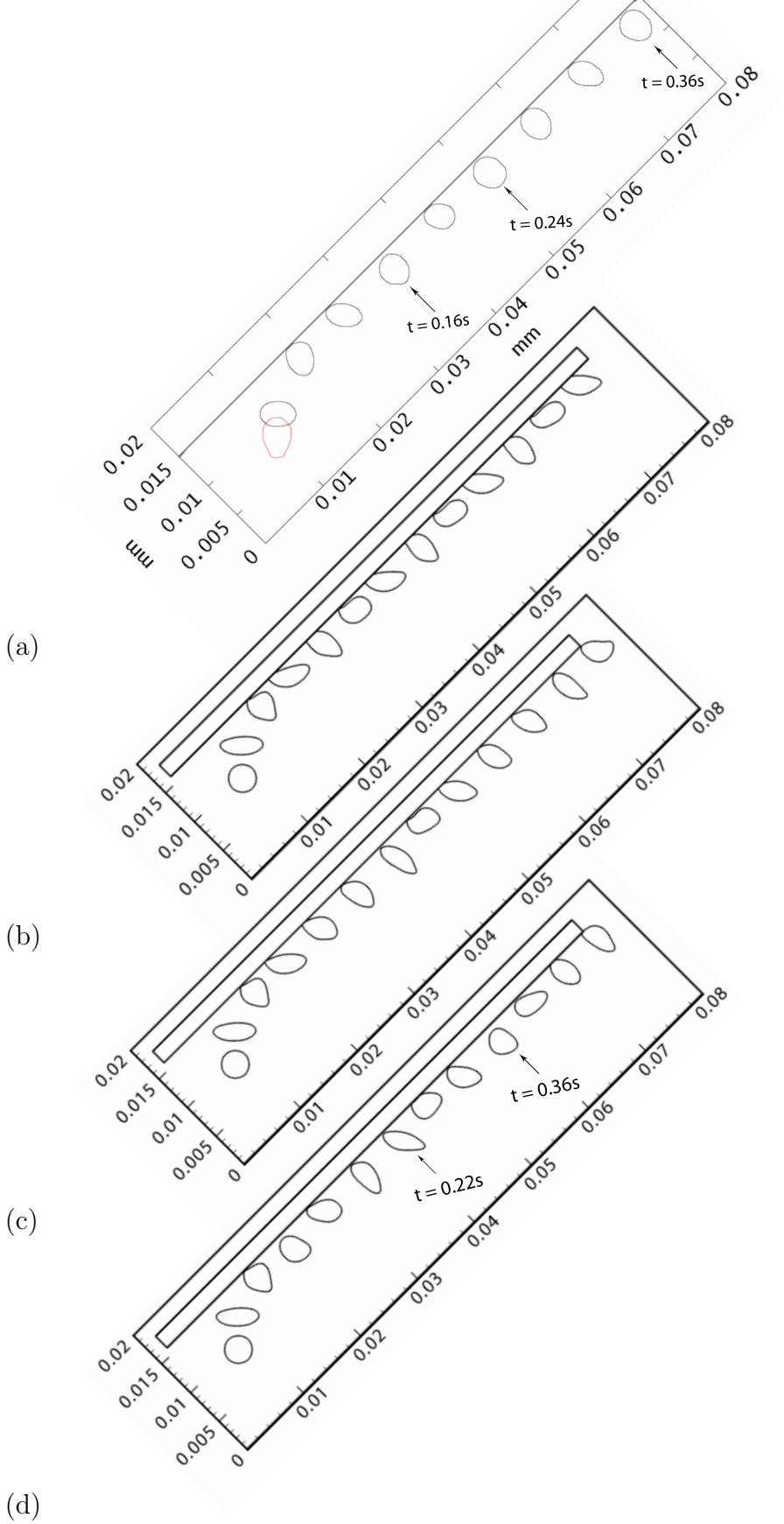

Figure 8: Bubble interface plots with plate inclination angle $\theta = 45°$ at time intervals $\Delta t = 0.04s$; (a) Experimental; Computational with varying contact angle (b) $\theta_c = 20^o$, (c) $\theta_c = 25^o$ and (d) $\theta_c = 30^o$.

of the cell adjacent to the surface. This will be noticeably slower than at a few cells removed from the surface and the effect is the observed reduction in the bubble velocity when it is in contact with the surface. The experimental bubble velocity is also significantly larger over most of the slide (see Fig. 7). The velocity first peaks after collision with a magnitude of $0.25m/s$ instead of $0.166m/s$ in all computations. Experimental results at lower plate inclination gave peaks of similar order of magnitude varying from $0.207m/s$ with $\theta = 10^\circ$ to $0.218m/s$ with $\theta = 30^\circ$. What is different in this case when compared to lower plate inclination measurements is the fact that the bubble does not slow down after this first peak but its velocity continues to oscillate with several peaks at about $0.22m/s$. Although the amplitude of velocity oscillations is generally larger in the numerical case, similar variations are measured experimentally. Towards the end of the measurement window however, the experimental bubble velocity decreases significantly as the bouncing component vanishes. It can be seen, by correlating the velocity to the interface contour plots, that the numerical velocity peaks when the bubble detaches from the surface that is when the interface does not connect with the solid surface. The numerical bubble velocity is then seen to approach the mean experimental velocity, reflecting again the drag effect due to the contact angle formulation. See for example the circled peaks in Fig. 7 and the corresponding bubble position in Fig. 8.d.

A last observation relates to the shape of the bubble when fully detached from the surface as a result of the bounce. In this case the computational and experimental contour plots show good agreement. This suggests that the suitability of the VOF-CSF method as confirmed by studies of single bubbles in free rise ((4), (5)) can be quickly recovered once the influence of the boundary condition is reduced.

5. Conclusion

The impact and slide of an ellipsoidal air bubble of 3.4mm equivalent diameter along an inclined plate was studied to assess the validity of the static contact angle boundary condition in a VOF-CSF formulation for accurate modelling of bubbles of low Eötvös and Morton Number. This was achieved by varying the inclination angle of the solid surface from 10° to 45° and assessing computational results with reference to experimental measurements and observations. Three static contact angles $\theta_c = \{20^\circ, 25^\circ, 30^\circ\}$ were tested for each plate inclination. Several conclusions can be drawn from this study.

- The dependence of mean slide velocity on surface tension is most significant at low plate inclination when the inertia, drag and surface tension forces are of similar magnitude with up to 22% difference ($\theta_c = 20^\circ$ used as reference) in the modelled terminal slide velocity.

- Increasing the static contact angle stretches a bubble in the direction perpendicular to the solid surface when it is in contact with a solid surface. This is observed for all plate inclinations but at higher inclinations significant changes to the bubble dynamics results from increase of as little as 5° in the contact angle. As the bubble reaches higher velocities with increased plate inclination, this stretching is shown to promote bubble deformation leading to bubble detachment from the surface. This detachment occurs at lower plate inclination than expected from experiments.

- A bubble which is detached from the surface accelerates rapidly reaching a velocity which agrees well with experimental measurements, whereas a sliding bubble tends to be at lower velocity. This can be attributed to a reduction in pressure drag experienced by the bubble which is allowed to deform more freely when its interface is not constrained by the wall boundary condition. Also as the bubble bounces away from the surface the no-slip boundary condition will have a lower impact on magnitude of interface advection. Once brought back in contact with the wall under the action of buoyancy the bubble slows down until it detaches again leading to a periodic bouncing trajectory and corresponding oscillations in the bubble velocity. Similar repeated bouncing is known to characterise ellipsoidal bubbles sliding under inclined flat surfaces but the static contact angle has been shown to promote early lift off.

- The static contact angle does not maintain the thin lubrication film between the bubble and the surface and instead assumes that the bubble interface intersect the plate surface as soon as it is in a cell adjacent to the wall. This was shown to hold the bubble back under certain conditions for some contact angles. At the initial impact with the wall the bubble is forced against the wall and a change in the contact angle is found to have a limited effect on the velocity or bubble shape. However, once the bubble accelerates under buoyancy after impact, it is clearly shown to be held back (slowed down) by the part of its interface which is in contact with the wall. This is particularly noticeable at the lower

contact angles which do not promote lift off and is clearly linked to a lower bubble slide velocity.

- when the bubble detaches from the surface as it bounces during the slide, good agreement between the experimental and predicted bubble shape and velocity are observed.

Acknowledgements

This research was supported by the Irish Research Council for Science Engineering and Technology under its Embark Initiative Basic Research Grant Scheme (grant number SC/2004/E0077) as well as Science Foundation Ireland under its Research Frontiers Programme (grant number 09/RFP/ENM2151). Additional measurements were performed by David Brendan Donoghue of the Department of Mechanical and Manufacturing Engineering, Trinity College Dublin, Ireland.

References

[1] M. Cook, M. Behnia, Bubble motion during inclined intermittent flow, International Journal of Heat and Fluid Flow 22 (5) (2001) 543–551. doi:10.1016/s0142-727x(01)00113-8.

[2] H. Tsao, D. Koch, Observations of high reynolds number bubbles interacting with a rigid wall, Physics of Fluids 9 (1) (1997) 44–56.

[3] G. Yang, B. Du, l.S. Fan, Bubble formation and dynamics in gas-liquid-solid fluidization–a review, Chemical Engineering Science 62 (1-2) (2007) 2 – 27, fluidized bed applications. doi:10.1016/j.ces.2006.08.021.

[4] Tomiyama, A and Sou, A and Minnagawa, H and Sakaguchi, T, Numerical analysis of a single bubble by a vof method, JSME International Journal Series B-Fluids and Thermal Engineering 36 (1) (1993) 51–56.

[5] D. Gueyffier, J. Li, A. Nadim, R. Scardovelli, S. Zaleski, Volume-of-fluid interface tracking with smoothed surface stress methods for three-dimensional flows, Journal of Computational Physics 152 (2) (1999) 423–456.

[6] E. Roitberg, L. Shemer, D. Barnea, Hydrodynamic characteristics of gas-liquid slug flow in a downward inclined pipe, Chemical Engineering Science 63 (14) (2008) 3605–3613. doi:10.1016/j.ces.2008.04.034.

[7] C.-W. Kang, S. Quan, J. Lou, Numerical study of a taylor bubble rising in stagnant liquids, Physical Review E 81 (6, Part 2). doi:10.1103/PhysRevE.81.066308.

[8] M. Kawaji, J. DeJesus, G. Tudose, Investigation of flow structures in vertical slug flow, Nuclear Engineering and Design 175 (1-2) (1997) 37–48.

[9] T. Maxworthy, Bubble rise under an inclined plate, Journal of Fluid Mechanics 229 (1991) 659–673.

[10] Y. Delaure, V. Chan, D. Murray, A simultaneous piv and heat transfer study of bubble interaction with free convection flow, Experimental Thermal and Fluid Science 27 (8) (2003) 911–926. doi:10.1016/S0894-1777(03)00070-0.

[11] J.-b. Dupont, D. Legendre, Numerical simulation of static and sliding drop with contact angle hysteresis, Journal of Computational Physics.

[12] M. Renardy, Y. Renardy, J. Li, Numerical simulation of moving contact line problems using a volume-of-fluid method, Journal of Computational Physics 171 (1) (2001) 243 – 263. doi:10.1006/jcph.2001.6785.

[13] C. Hirt, B. Nichols, Volume of fluid (vof) method for the dynamics of free boundaries, Journal of Computational Physics 39 (1) (1981) 201–225.

[14] M. Sussman, P. Smereka, S. Osher, A level set approach for computing solutions to incompressible 2-phase flow, Journal of Computational Physics 114 (1) (1994) 146–159.

[15] J. Brackbill, D. Kothe, C. Zemach, A continuum method for modeling surface-tension, Journal of Computational Physics 100 (2) (1992) 335–354.

[16] C. Norman, M. Miksis, Dynamics of a gas bubble rising in an inclined channel at finite Reynolds number, Physics of Fluids 17 (2). doi:10.1063/1.1842220.

[17] W. Rider, D. Kothe, Reconstructing volume tracking, Journal of Computational Physics 141 (2) (1998) 112–152.

[18] S. Patankar, Numerical Heat Transfer and Fluid Flow, Series in Computational and Physical Processes in Mechanics and Thermal Sciences, Taylor & Francis, 1980.

[19] C. de Boor, A practical guide to splines, Applied mathematical sciences; 27, Springer-Verlag, 1978.

[20] Y. T.L., Time-dependent multi-material flow with large fluid distortion, in: M. KW, B. MJ (Eds.), Numerical Methods for Fluid Dynamics, 1982, pp. 273–285.

[21] R. Clift, J. Grace, M. Weber, Bubbles, Drops and Particles, Academic Press, U.K., 1978.